Biofunctionalization of selective laser melted porous titanium using silver and zinc nanoparticles to prevent infections by antibiotic-resistant bacteria

van Hengel, I. A.J.; Putra, N. E.; Tierolf, M. W.A.M.; Minneboo, M.; Fluit, A. C.; Fratila-Apachitei, L. E.; Apachitei, I.; Zadpoor, A. A.

Important note
To cite this publication, please use the final published version (if applicable).
Please check the document version above.

Full length article

Biofunctionalization of selective laser melted porous titanium using silver and zinc nanoparticles to prevent infections by antibiotic-resistant bacteria

I.A.J. van Hengel [a,*], N.E. Putra [a], M.W.A.M. Tierolf [a], M. Minneboo [a], A.C. Fluit [b], L.E. Fratila-Apachitei [a], I. Apachitei [a], A.A. Zadpoor [a]

[a] *Additive Manufacturing Laboratory, Department of Biomechanical Engineering, Faculty of Mechanical, Maritime, and Materials Engineering, Delft University of Technology, the Netherlands*
[b] *Department of Medical Microbiology, University Medical Center Utrecht, Utrecht, the Netherlands*

ABSTRACT

Antibiotic-resistant bacteria are frequently involved in implant-associated infections (IAIs), making the treatment of these infections even more challenging. Therefore, multifunctional implant surfaces that simultaneously possess antibacterial activity and induce osseointegration are highly desired in order to prevent IAIs. The incorporation of multiple inorganic antibacterial agents onto the implant surface may aid in generating synergistic antibacterial behavior against a wide microbial spectrum while reducing the occurrence of bacterial resistance. In this study, porous titanium implants synthesized by selective laser melting (SLM) were biofunctionalized with plasma electrolytic oxidation (PEO) using electrolytes based on Ca/P species as well as silver and zinc nanoparticles in ratios from 0 to 100% that were tightly embedded into the growing titanium oxide layer. After the surface bio-functionalization process, silver and zinc ions were released from the implant surfaces for at least 28 days resulting in antibacterial leaching activity against methicillin-resistant *Staphylococcus aureus* (MRSA). Furthermore, the biofunctionalized implants generated reactive oxygen species, thereby contributing to antibacterial contact-killing. While implant surfaces containing up to 75% silver and 25% zinc nanoparticles fully eradicated both adherent and planktonic bacteria *in vitro* as well as in an *ex vivo* experiment performed using murine femora, solely zinc-bearing surfaces did not. The minimum inhibitory and bactericidal concentrations determined for different combinations of both types of ions confirmed the presence of a strong synergistic antibacterial behavior, which could be exploited to reduce the amount of required silver ions by two orders of magnitude (*i.e.*, 120 folds). At the same time, the zinc bearing surfaces enhanced the metabolic activity of pre-osteoblasts after 3, 7, and 11 days. Altogether, implant biofunctionalization by PEO with silver and zinc nanoparticles is a fruitful strategy for the synthesis of multifunctional surfaces on orthopedic implants and the prevention of IAIs caused by antibiotic-resistant bacteria.

Statement of Significance

Implant-associated infections are becoming increasingly challenging to treat due to growing antibiotic resistance against antibiotics. Here, we propose an alternative approach where silver and zinc nanoparticles are simultaneously used for the biofunctionalization of rationally designed additively manufactured porous titanium. This combination of porous design and tailored surface treatment allows us to reduce the amount of required silver nanoparticles by two orders of magnitude, fully eradicate antibiotic-resistant bacteria, and enhance the osteogenic behavior of pre-osteoblasts. We demonstrate that the resulting implants display antibacterial activity *in vitro* and *ex vivo* against methicillin-resistant *Staphylococcus aureus*.

1. Introduction

Implant-associated infections (IAIs) are one of the main causes of implant failure [1,2]. IAIs are initiated by bacterial invasion of the wound cavity and the subsequent adherence of bacteria onto the implant surface [3]. This is usually followed by the formation of bacterial biofilms that make it extremely difficult to eradicate bacteria from the implant surface, as they become largely insusceptible to the antibacterial agents that, in order to be effective, would have to penetrate through the protective biofilm layer [4,5]. This is particularly concerning given the ongoing development of antibiotic resistance in bacterial species such as methicillin-resistant *Staphylococcus aureus* (MRSA) that has resulted in an increasing number of untreatable infections and significant patient mortality [6–10]. There is, therefore, an urgent need for the development of novel antibacterial strategies that minimize the risk of such infections.

There are two major strategies that could be used to minimize the risk of IAIs caused by antibiotic-resistant strains. The first strategy is to minimize the risk of biofilm formation by stimulating the fast regeneration of bony tissue. Driven by host cells that cover the implant surface at an early stage, the formation of *de novo* bone could result in full integration of the implant inside the host tissue. The additive manufacturing (AM) of geometrically complex and highly ordered porous implants can be particularly useful in enhancing the bone tissue regeneration performance of biomaterials by offering both an interconnected porous structure [11] and bone-mimicking mechanical properties [12,13]. Furthermore, such porous structures significantly increase the surface area that is available for the biofunctionalization of the implants. This increased surface area boosts the efficacy of the second strategy where the surface of the implant is biofunctionalized using combinations of potent antibacterial agents against which bacteria cannot easily develop resistance.

Here, we merged both of the aforementioned strategies to design and manufacture porous metallic implants to maximize the likelihood of preventing IAIs caused by antibiotic-resistant strains. Our approach consists of AM porous titanium using a rationally designed porous structure [14], which is then surface-biofunctionalized using plasma electrolytic oxidation (PEO) to create multifunctional surfaces that promote the osseointegration of the implants while exhibiting a potent antibacterial behavior against antibiotic-resistant bacteria. More specifically, the electrolyte used in the PEO process contained both Ca/P species that are known to elicit an osteogenic response [15] and two types of inorganic nanoparticles (*i.e.*, silver and zinc). The choice of the nanoparticles (NPs) is of crucial importance in this regard. Silver ions are highly potent agents against a very wide spectrum of bacterial strains [16–18]. Moreover, resistance against silver is rare and difficult to acquire [19]. Combining silver with zinc offers several advantages. First, we hypothesized that silver and zinc exhibit a synergistic behavior, providing the same level of bactericidal behavior with a much lower concentration of silver ions. This is particularly important given the concerns that high concentrations of silver ions could lead to cytotoxicity against host cells [20]. Second, combining several antibacterial agents that target the different components of bacterial cells [21,22] could further reduce the risk of bacterial resistance. Finally, certain concentrations of zinc ions are known to give rise to osteogenic behavior [23,24]. This could further reinforce the multifunctional performance of the implants.

During PEO, both Zn and Ag nanoparticles are tightly embedded in a growing TiO_2 surface layer that covers the entire surface of the porous titanium implants. Moreover, the PEO process generates a highly porous oxide layer that further expands the already vast surface area of the implants and enhances the release of ions from the incorporated elements [25–27].

In this study, we synthesized multifunctional AM implants and studied their surface characteristics, chemical composition and their performance against antibiotic-resistant bacteria using both *in vitro* and *ex vivo* assays. Moreover, we explored the mechanisms of their antibacterial behavior by evaluating the ion release kinetics and the generation of reactive oxygen species (ROS). Finally, we investigated the response of host cells to the implants through *in vitro* cultures of pre-osteoblasts and the assessment of their metabolic and alkaline phosphatase (ALP) activities.

2. Materials and methods

2.1. Implant design and additive manufacturing

We aimed to manufacture titanium implants suitable for testing in an *ex vivo* murine infection model. Therefore, we designed a hexagonal unit cell that was subsequently stacked to create implants with a length of 4 cm and a diameter of 5 mm. Subsequently, the implants were produced at the Additive Manufacturing Laboratory (TU Delft, Delft, The Netherlands) using a selective laser melting (SLM) printer (SLM-125, Realizer, Borchem, Germany) that operated with a YLM-400-AC Ytterbium fiber laser (IPG Photonics Corporation, Oxford, United States) under an argon atmosphere with less than 0.2% oxygen. The parameters of the SLM process were as follows: a wavelength of 1070 ± 10 nm, an exposure time of 300 µs and a laser power of 96 W, resulting in a laser spot size of 145 µm. We used a layer thickness of 50 µm and medical-grade (grade 23, ELI) Ti-6AL-4 V powder (AP&C, Boisbriand, Quebec, Canada), which had a spherical morphology with particle sizes of 10–45 µm. After SLM, the loose powder particles were removed by vacuum cleaning and the implants were ultrasonicated subsequently in acetone, 96% ethanol, and demineralized water for 5 min each.

2.2. Plasma electrolytic oxidation

The surface of the implants was biofunctionalized by PEO in an electrolyte containing 0.15 M calcium acetate (Dr. Paul Lohmann GmbH, Emmerthal, Germany) and 0.02 M calcium glycerophosphate (Sigma-Aldrich, St. Louis, Missouri, United States) dissolved in demineralized water. In addition, Ag NPs and/or Zn NPs (both from Sigma-Aldrich, St. Louis, Missouri, United States) were dispersed in varying ratios with 3.0 g/l indicated as 100% in the electrolyte. This resulted in PEO biofunctionalized implants without NPs (PT), with 3.0 and 1.5 g/L Ag NPs (PT–Ag and PT–Ag 50, respectively), with 3.0 g/L Zn NPs (PT–Zn), and with both Ag and Zn NPs (PT–Ag Zn, PT–Ag Zn 75 25, and PT–Ag Zn 50 50). The as-manufactured implants (NT) served as a control group. Both Ag and Zn NPs displayed a spherical morphology with particle sizes ranging between 7 and 25 nm for Ag NPs and between 40 and 60 nm for Zn NPs. The PEO electrolyte was sonicated 2 times for 3 min and stirred in between for 5 min at 500 rpm on a magnetic stirrer (IKA-Werke GmbH & Co. KG, Staufen, Germany) using a stir bar of 40×8 mm (VWR, Radnor, Pennsylvania, United States).

The PEO process was performed using a custom-made laboratory setup that comprised an AC power supply (50 Hz, type ACS 1500, ET powder Systems Ltd., Chesterfield, United Kingdom), a data acquisition board (SCXI, National Instruments, Austin, Texas, United States), and two electrodes inside a double-walled glass electrolytic cell. During the PEO process, a ring-shaped piece made from stainless steel served as the cathode while the implant was the anode. The voltage-time (*V-t*) transients were recorded every second. PEO processing took place at a current density of 20 A/dm^2 under galvanostatic conditions in 800 ml electrolyte for 5 min while the electrolytic cell was cooled with a thermostatic bath to keep the temperature between 6–8 °C throughout the PEO process.

A homogeneous distribution of particles inside the electrolyte was established by continuously stirring at 500 rpm. Following PEO biofunctionalization, the implants were cleansed in running tap water for 1 min, sterilized at 110 °C for 1 h in an oven (Nabertherm TR60, New Castle, United States), and stored under sterile conditions.

2.3. Zeta potential of nanoparticles in PEO electrolyte

The stability of the Ag and/or Zn nanoparticles in the PEO electrolyte was determined by measurement of the zeta potential using a Zetasizer Nano ZS (Malvern Analytical, United Kingdom). The PEO electrolytes containing ratios of Ag and/or Zn nanoparticles from 0–100% were diluted 10 times and subsequently 1 mL was injected into a DTS1060 capillary cell ($n = 3$/condition). Thereafter, the zeta potential was determined at room temperature with 10 runs for each measurement.

2.4. Analysis of surface morphology, chemical composition and titanium oxide layer

The surface morphology of the biofunctionalized implants was imaged using scanning electron microscopy (SEM, JSM-IT100LV, JEOL, Tokyo, Japan). Prior to that, the implants were covered with a gold layer of 5 ± 2 nm to enhance their electrical conductivity. During SEM imaging an electron beam intensity ranged between 5–20 kV and working distance of 10 mm were used. By means of energy dispersive X-ray spectroscopy (EDS), the chemical composition on the surface of the implants was determined using spot analyses.

In addition, a cross-sectional analysis was performed to analyze the titanium oxide layer on the implant surface. Therefore, implants were sectioned perpendicular towards the longitudinal axis and embedded in a conductive resin with carbon filler (PolyFast, Struers, Copenhagen, Denmark). Subsequently, the specimens were grounded with sandpapers of 4000, 2000, 800, 320, 180 and 80 grit (Struers) under running tap water. Thereafter, the specimens were ultrasonicated for 5 min in isopropanol, dried in air, polished with 3 and 1 μm diamond suspension DiaDuo-2 (Struers) and analyzed by SEM. Furthermore, the chemical composition of the titanium layer was determined by EDS ($n = 5$).

2.5. Ion release kinetics

The release kinetics of Ag and Zn ions were determined by inductively coupled plasma – optical emission spectrometry (ICP-OES). Biofunctionalized implants of 1 cm in length were placed in dark Eppendorf tubes ($n = 3$/group) containing 1 mL phosphate-buffered saline (PBS). During the experiments, the specimens were kept at 37 °C using a water bath under static conditions. The PBS was collected and replenished after 0.5, 1, 2, 4, 7, 14, and 28 days. To dissolve all ions in the liquid, the collected PBS was acidified with 5% nitric acid. Subsequently, the ion concentration was detected by ICP-OES using a PerkinElmer Optima 3000DV (PerkinElmer, Zaventem, Belgium).

2.6. Electron paramagnetic resonance

The formation of ROS by the implants was determined through an electron paramagnetic resonance (EPR) spectrometer (Bruker EMX Plus, Billerica, Massachusetts, United States). The implants ($n = 2$/group) of 0.5 cm in length were inserted in a quartz capillary tube and placed inside the EPR spectrometer. Thereafter, the baseline spectra of the implants were determined followed by a measurement of the spectra corresponding to the radicals formed as a result of submerging the implants in 10 μl PBS containing 20 mM spin trap 5,5-dimethyl-pyrroline N-oxide (DMPO, Sigma-Aldrich, St. Louis, United States). The radical generation was analyzed every 10 min for 2.5 h with the following EPR settings: a frequency of 9.78 GHz, a sweep width of 100 G, a time constant of 163.8 ms, a conversion time of 160 ms, a modulation amplitude of 1 G, a modulation frequency of 100 kHz, a receiver gain of 60 dB, an attenuation of 10 dB, and a power of 20 mW.

2.7. Antibacterial assays

2.7.1. Preparation of the bacterial inoculum

The bactericidal properties of the biofunctionalized implants were assessed against MRSA USA300 [28] using in vitro and ex vivo assays. The bacterial inocula were prepared by resuspending a single colony into 3 mL tryptic soy broth (TSB) or cation-adjusted Mueller Hinton broth (CAMH) followed by incubation for 2 h at 37 °C while shaking at 120 rpm. Thereafter, the optical density at 600 nm (OD_{600}) was measured and the required bacterial inoculum was prepared. The inoculum was verified by plating 10 μL triplicates of 10-fold serial dilutions on blood agar plates (Becton Dickinson, Franklin Lakes, United States) followed by overnight incubation at 37 °C and colony forming unit (CFU) quantification.

2.7.2. Inhibition zone

The antibacterial leaching activity of the implants was determined using an inhibition zone assay. Luria broth (LB) containing 200 g tryptone, 100 g yeast powder, 240 g Agar No.1 (all from Oxoid, ThermoFisher Scientific, Massachusetts, United States) and 200 g NaCl dissolved in 20 L ultrapure water was used to pour agar plates. A bacterial inoculum of 10^7 CFU/mL in TSB was distributed over the agar plates using a cotton swab and subsequently 1.5 cm implants ($n = 3$/group) were pressed onto the agar surface and incubated in a humid environment at 37 °C for 24 h. Following incubation, the area of the inhibition zones was determined by an image processing program (Photoshop CS6, Adobe, California, United States) to determine the antibacterial leaching activity of the specimens.

2.7.3. Minimal inhibitory concentration (MIC) and minimal bactericidal concentration (MBC)

The MIC and MBC of Ag^+ and Zn^{2+} ions, as well as combinations thereof, against MRSA USA300 were determined using Ag nitrate and Zn nitrate (both from Sigma-Aldrich, St. Louis, United States) dissolved in CAMH broth. Next, two-fold serial dilutions were prepared in 96-well plates starting at initial concentrations of 2 mM for Ag^+ and 80 mM for Zn^{2+}, respectively. Subsequently, an inoculum at OD_{600} 0.09 was prepared of which 65 μL was transferred to 10 mL of CAMH. Next, 50 μL of the bacterial inoculum and 50 μL of both Ag^+ and Zn^{2+} dilutions were added to a 96-well plate and incubated overnight at 37 °C under static conditions. Following incubation, the MIC was denoted as the lowest concentration of Ag^+ and/or Zn^{2+} where no turbidities were observed. The MBC was determined using 10 μL aliquots of each well plated on blood agar plates and overnight incubation at 37 °C. The MBC was determined as the lowest concentration of Ag^+ and/or Zn^{2+} ions without any bacterial colonies present.

2.7.4. Quantification of adherent and planktonic bacteria on implants

The bactericidal activity of the biofunctionalized implants was quantified for both adherent and planktonic bacteria against a bacterial inoculum of $2 \times 10^{10^3}$ CFU MRSA USA300 in 100 μL TSB + 1% glucose in a 200 μL MicroAmp® Fast Reaction Tube (Life Technologies, Carlsbad, California, United States) to which 4 implants of 1 cm in length were added. The specimens ($n = 3$/group)

were incubated overnight under static conditions at 37 °C. Subsequently, the number of the adherent CFU was quantified by rinsing the specimens 3 times in PBS and ultrasonication in 200 µL PBS for 3 min of which 10 µL aliquots of subsequent 10-fold serial dilutions were plated on blood agar plates. The non-adherent bacteria present in the culture medium were quantified by plating 10 µL of 10-fold dilutions onto blood agar plates followed by CFU quantification after overnight incubation at 37 °C.

2.7.5. Biofilm formation and characterization

The ability of the implants to prevent biofilm formation ($n = 2$/group) was determined through static incubation in 100 µL TSB + 1% glucose with 2×1010^3 CFU/mL MRSA USA300 at 37 °C for 24 h. After 24 h, the implants were rinsed in PBS and fixated in McDowels fixative (4% paraformaldehyde and 1% glutaraldehyde in 10 mM phosphate buffer at pH 7.4). Subsequently, the fixated implants were dehydrated using the following procedure: rinsing in demineralized water for 5 min, dehydrating in 50% ethanol for 15 min, 70% ethanol for 20 min, 96% ethanol for 20 min, and hexamethyldisilazane for 15 min. Thereafter, the implants were left to dry in air for 2 h, sputtered with a gold layer of 5 ± 2 nm, and analyzed by SEM.

2.7.6. Ex vivo infection model

The antibacterial properties of the specimens were also studied in an *ex vivo* infection model using murine femurs provided by the Central Laboratory Animal Institute (Utrecht University). First, the tissues surrounding the femurs were removed. Then, the femurs were sterilized using 70% ethanol for 10 min and were subsequently submerged in demineralized water for 10 min. A hole of 0.5 mm was drilled through the epicondyle into the intramedullary canal. The bone marrow was removed with a syringe, and 2 µL of PBS was inserted into the medullary cavity. Prior to implantation, the implants were inoculated with 200 CFU MRSA USA300 in 2 µL demineralized water, dried in air for 15 min, and press-fitted into the femur.

To verify the proper sterilization, one femur was not implanted with an implant (negative control). The model was validated by injecting 2 µL tetracycline (50 mg/mL, Sigma-Aldrich, St. Louis, Missouri, United States) intramedullary before implantation with an inoculated NT implant. Following the implantation procedure, the femurs were inserted in 0.5 mL Eppendorf tubes and were incubated on a dynamic platform to simulate intraosseous fluid flow at 37 °C for 24 h. After overnight incubation, the femurs were homogenized using 15 zirconia beads (Ø 2 mm, BioSpec, Bartlesville, Oklahoma, United States) in 800 µl PBS with a MagNA Lyser (Roche Diagnostics, Risch-Rotkreuz, Switzerland) at 7000 rpm for 2 rounds of 30 s each while being cooled on ice in between. To quantify the number of CFU, 10-fold serial dilutions of the homogenate were plated on blood agar plates and incubated overnight at 37 °C.

2.8. Cytocompatibility of MC3T3-E1 cells on implants

2.8.1. Pre-culture of cells and cell seeding

Pre-osteoblast MC3T3-E1 cells (Sigma-Aldrich) were cultured for 7 days in α-MEM supplemented with 1% penicillin-streptomycin and 10% fetal bovine serum (all from ThermoFisher, Waltham, Massachusetts, United States). The medium was refreshed every 2–3 days. For cell seeding on 1 cm implants, 1.5×10^5 MC3T3-E1 cells were added to 100 µL culture medium in 0.2 mL tubes. To stimulate cell adhesion, the implants were tilted every 20 min for 2 h in total (37 °C, 5% CO_2) and were thereafter placed in a 48 well plate with 200 µL fresh medium. After 2 days, osteogenic differentiation was initiated by the addition of 50 µg/µL ascorbic acid and 4 mM β-glycerophosphate (both

from Sigma-Aldrich). During the experiments, the culture medium was refreshed every 2 – 3 days.

2.8.2. Presto blue assay

The metabolic activity of the MC3T3-E1 cells was determined after 1, 3, 7, and 11 days using a PrestoBlue assay (Thermofisher, Waltham, MA, United States). The implants were incubated in 200 µL fresh culture medium for 1 h at 37 °C with 20 µL PrestoBlue cell viability reagent. Subsequently, the absorbance was measured at a wavelength of 530–590 nm with a Wallac plate reader (Victor X4, PerkinElmer, Massachusetts, United States).

2.8.3. Alkaline phosphatase (ALP) assay

The ALP activity of the MC3T3-E1 cells was determined after 11 days by rinsing the implants ($n = 4$/group) with PBS and submersion in 250 µL PBS-Triton (8% NaCl, 0.2% KCl, 1.44% Na_2HPO_4, 0.24% KH_2PO_4, and 0.1% Triton X-100 in H_2O). To dissociate the cells, the implants were ultrasonicated for 10 s and incubated for 10 min at 37 °C in 100 µL p-nitrophenyl phosphate (pNPP, Sigma-Aldrich). The enzymatic reaction was blocked with the addition of 250 µL NaOH. The absorbance at a wavelength of 405 nm was then measured with a Wallac plate reader (Perkin Elmer). To determine the ALP activity, a standard curve was prepared through the addition of 100 µL PBS-Triton and 250 µL NaOH to each well. The total protein content was determined with a BSA protein assay kit (Invitrogen). Subsequently, the ALP levels were normalized to the total protein content.

2.8.4. Morphology of MC3T3-E1 cells on implants

The implants with MC3T3-E1 cells were fixated after 11 days in McDowels fixative (4% paraformaldehyde and 1% glutaraldehyde in 10 mM phosphate buffer at pH 7.4) and were stored at 4 °C. Subsequently, the implants were cleansed twice for 5 min in demineralized water and were dehydrated using an ethanol dilution series of 15 min in 50%, 20 min in 70%, and 20 min in 96%. Next, the implants were dried in air for 2 h, sputtered with a gold layer of 5 ± 2 nm, and analyzed by SEM ($n = 2$/group).

2.9. Statistical analysis

All data are expressed as mean $\pm$ standard deviation. The statistical analyses were performed using GraphPad Prism (GraphPad Software, La Jolla, California, United States) with one-way ANOVA and Bonferroni *post hoc* test. The differences between groups were considered statistically significant at $p < 0.05$.

3. Results

3.1. PEO biofunctionalization and surface morphology of Ti6Al4V implants

Following SLM, the porous implants displayed partially molten or unmolten Ti-6Al-4V powder particles tightly attached to their surface (Fig. 1A). Subsequently, the implants were biofunctionalized in a PEO setup (Fig. 1B) using Ca/P-based electrolytes with Ag and/or Zn NPs. The addition of NPs to the PEO electrolyte did not affect the *V-t* curves obtained during the PEO process (Fig. 1C). Prior to dielectric breakdown, the voltage increased with 14 ± 1 V/s followed by an inflection of the curve and a decreased rate of growth of 0.49 V/s. From 115 ± 5 V, plasma discharges were observed until a final voltage of 249 ± 6 V was reached. The zeta potential of Ag and/or Zn NPs in the PEO electrolyte varied between −11 to −20 mV, demonstrating a negative charge of the NPs in the electrolyte (Fig. 1D). Surface characterization by SEM revealed a homogenous micro-/nano-porous oxide layer on the outer
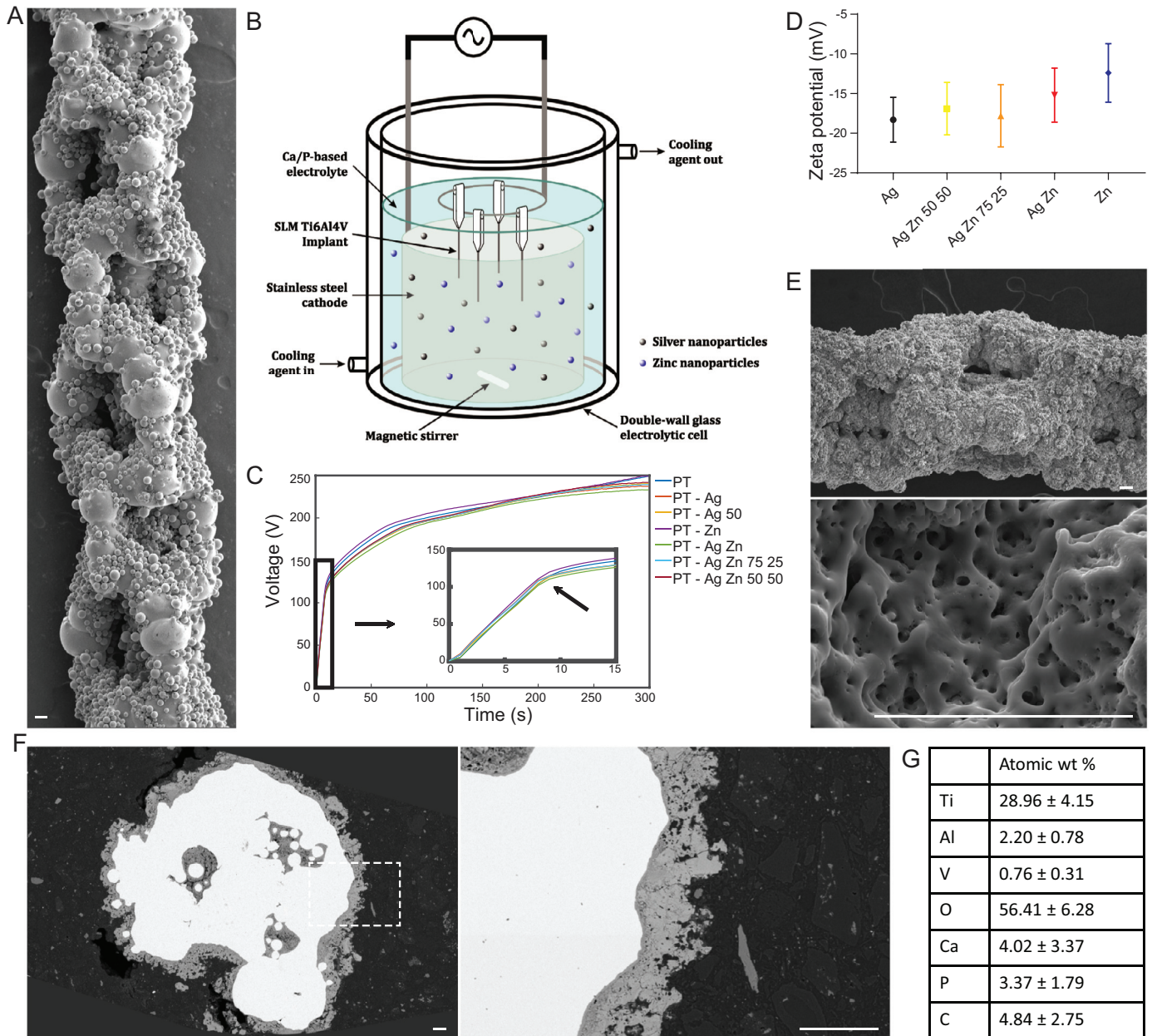
Fig. 1. (A) The surface morphology of selective laser melted Ti-6Al-4V implants imaged using SEM. (B) An illustration of the electrolytic cell used for PEO biofunctionalization depicting the electrolyte, Ag and Zn nanoparticles, the arrangement of the implants, and cathode. (C) The V-t curves recorded during the PEO biofunctionalization of the SLM implants with different electrolytes containing the varying ratios of Ag and/or Zn NPs. (D) Zeta potential measurements of Ag and/or Zn NP ratios dispersed in the PEO electrolyte. (E) SEM images of the surface morphology of a PT implant following 300 s of PEO biofunctionalization. (F) Cross-sectional analysis of a biofunctionalized implant by SEM. (G) Chemical composition of the titanium oxide layer determined by EDS ($n = 5$). Scale bar = 50 μm.

surface of the implants (Fig. 1E). Furthermore, the surface morphology of implants bearing Ag and/or Zn NPs did not differ from the PT implants. Cross-sectional analysis of the implants by SEM demonstrated the presence of a titanium oxide layer on both the inner and the outer surface of the implants (Fig. 1F). In the oxide layer the presence of Ti, Al, V, O, Ca, P and C elements was confirmed by EDS (Fig. 1G).

3.2. Surface chemistry and phase composition

Following PEO processing, Ag and Zn NPs were observed on the implant surfaces as demonstrated by EDS analysis (Fig. 2). Ag and/or Zn NPs were fully embedded onto the TiO_2 surface layer and were widely spread. EDS point analysis indicated the presence

of Ca, P, Ti, Al, and V on the surface of all biofunctionalized implants while Ag and/or Zn NPs were found for PT–Ag, PT–Zn, and PT–Ag Zn implant surfaces, respectively.

3.3. Ion release kinetics and formation of reactive oxygen species

3.3.1. Ion release kinetics

Combining Ag and Zn NPs resulted in a reduced rate of Ag ion release in the first 24 h for the PT–Ag Zn, PT–Ag Zn 50 50, and PT–Ag 50 groups as compared to the PT–Ag implants ($p < 0.001$; Fig. 3A). The release of Zn ions was not affected by the incorporation of Ag NPs onto the implant surface (Fig. 3B). The release of the ions persisted up to at least 28 days. Combining Ag and Zn NPs reduced the release of Ag ions from the PT–Ag Zn, PT–Ag Zn
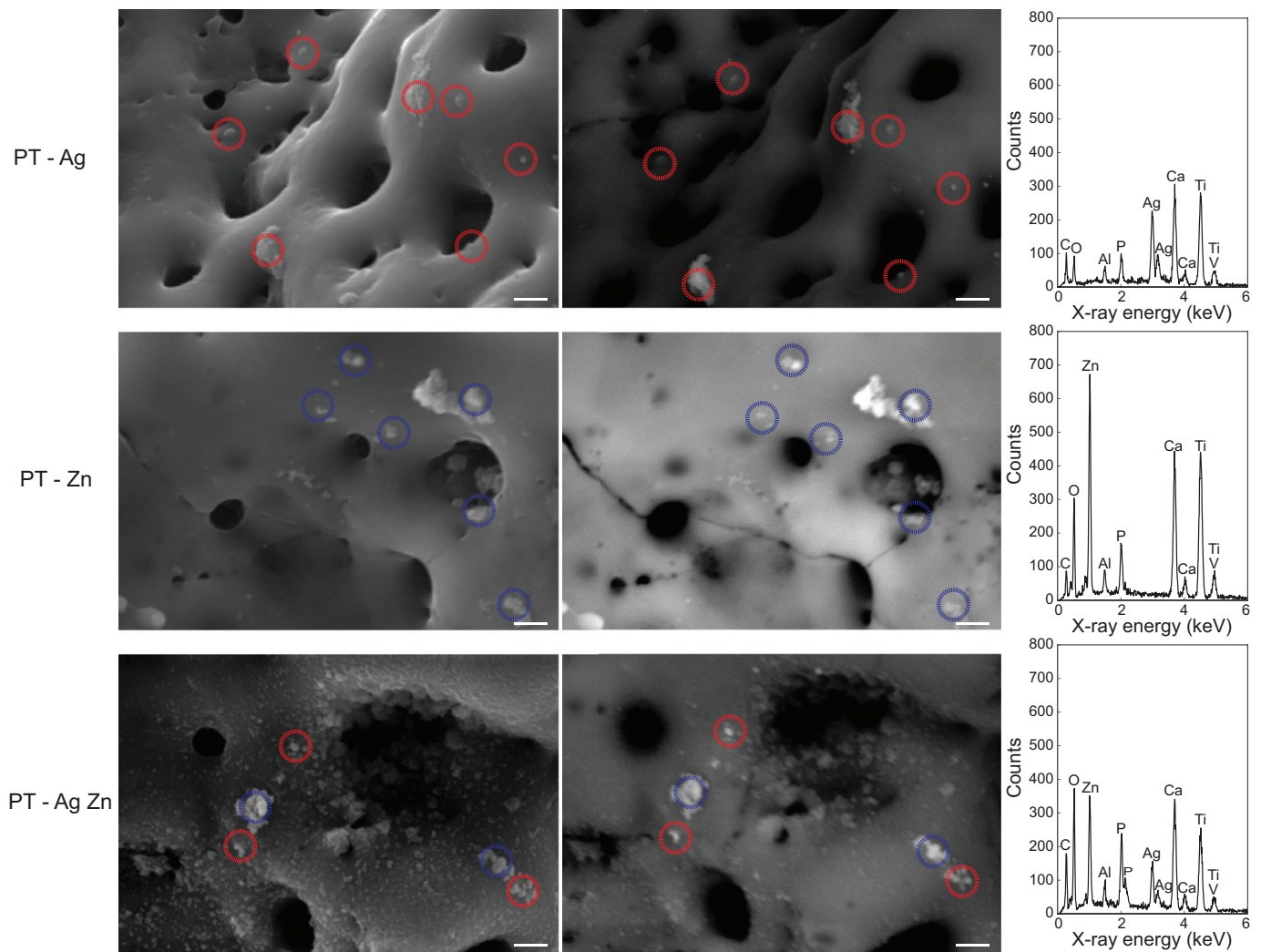
Fig. 2. EDS analysis of the biofunctionalized implants containing Ag and/or Zn NPs. The locations of the Ag NPs (red circles) and Zn NPs (blue circles) on the implant surface were demonstrated using secondary (left) and backscattered (right) SEM images. EDS spot analysis confirmed the presence of Ag and Zn NPs as part of a surface layer consisting of Ti, Al, V, C, O, Ca, and P. Scale bar = 1 μm. (For interpretation of the references to colour in this figure legend, the reader is referred to the web version of this article.)

75 25, and PT–Ag Zn 50 50 groups as compared to the PT–Ag implants ($p < 0.001$, $p < 0.05$, and $p < 0.001$, respectively; Fig. 3C) while the release of Zn ions was enhanced for the PT–Zn implants as compared to the PT–Ag Zn 50 50 group ($p < 0.05$; Fig. 3D).

3.3.2. Reactive oxygen species formation

Both hydroxyl and methyl radicals were generated by all of the biofunctionalized implant groups, while NT implants did not generate any ROS (Fig. 3E). Following the hydroxyl radical formation for up to 2.5 h, the PT–Zn group exhibited a higher level of radical formation as compared to all other groups (Fig. 3F).

### 3.4. Antibacterial assays

3.4.1. Antibacterial leaching activity and minimal inhibitory and bactericidal concentration

Following 24 h incubation, the implants bearing Ag NPs demonstrated zones of inhibition whereas the NT, PT, PT–Zn and PT–Zn implants showed no such zones (Fig. 4A). The size of the inhibition zones was similar between the implants indicating that the antibacterial leaching activity did not differ significantly (Fig. 4B). The synergistic effects on antibacterial activity between Ag$^+$ and

Zn^{2+} ions were studied by determining the MIC and MBC for Ag$^+$ and Zn^{2+} against MRSA USA300. The MIC was 4 μM for Ag$^+$ and 630 μM for Zn^{2+} while combining 2 μM Ag$^+$ and 310 μM Zn^{2+} fully prevented bacterial growth (Fig. 4C). Similarly, the MBC was respectively 60 μM and 5000 μM for Ag$^+$ and Zn^{2+} while combining 30–0.47 μM Ag$^+$ with 160–2500 μM Zn^{2+} resulted in total eradication of the bacterial inoculum (Fig. 4D).

3.4.2. Quantification of bactericidal activity and biofilm prevention

The specimens from the PT–Ag, PT–Ag 50, PT–Ag Zn, and PT–Ag Zn 75 25 groups totally prevented bacterial adhesion whereas those from the PT–Ag Zn 50 50 group showed a four-log inhibition ($p < 0.001$) as compared to the specimens from the NT, PT, and PT–Zn groups (Fig. 4E). Similar results were obtained for planktonic bacteria with the PT–Ag Zn 50 50 group demonstrating a two-log inhibition ($p < 0.001$) as compared to the NT, PT, and PT–Zn implants (Fig. 4F). The NT, PT, and PT - Zn implants did not prevent biofilm formation on the implants where bacteria were observed to be on top of each other in multiple layers (Fig. 5). The PT–Ag and PT–Ag Zn implants, on the other hand, rarely displayed any attached bacteria. In the rare occasions where bacteria were found
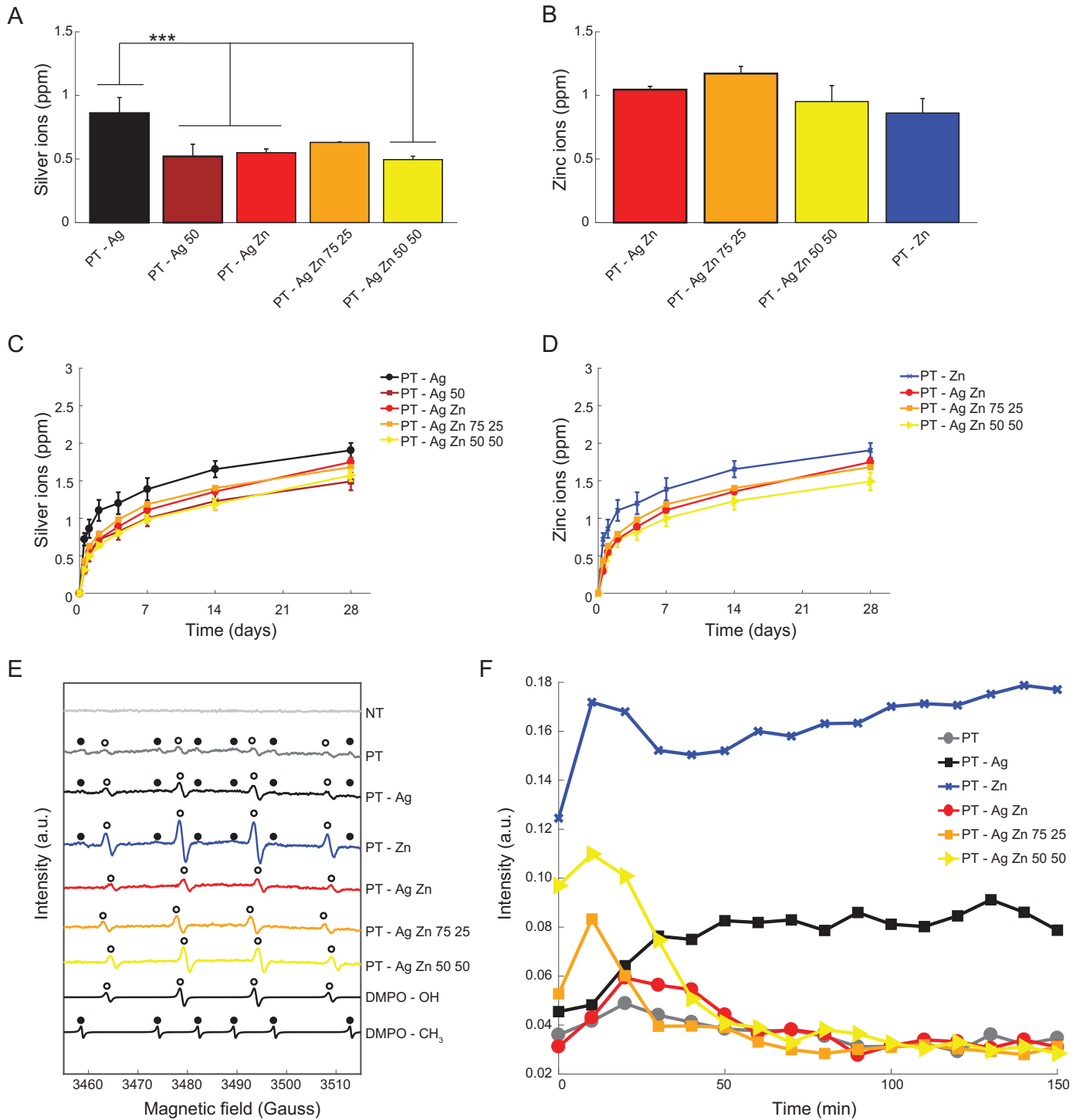
Fig. 3. The ion release profile and the generation of ROS. (A) The Ag and (B) Zn ions released from the biofunctionalized implants ($n = 3$) after 24 h in PBS as measured by ICP-OES. The cumulative release profile of (C) Ag and (D) Zn ions measured during a period of 28 days. (E) The generation of ROS by the implants as measured by electron paramagnetic resonance using DMPO spin trap. DMPO – OH and DMPO – CH$_3$ depict a simulation of OH and CH$_3$ radical spectra respectively. (F) The 2D electron paramagnetic resonance spectrum measured for the hydroxyl radical formation for up to 150 min. *, $p < 0.05$, **, $p < 0.01$, ***, $p < 0.001$.

on the surface of the PT–Ag and PT–Ag Zn implants, they were primarily observed inside the PEO micropores.

3.4.3. Ex vivo antibacterial activity

The *ex vivo* bactericidal activity of the implants was evaluated in a murine femoral infection model (Fig. 6A). After 24 h of incubation, the PT–Ag, PT–Ag Zn and PT–Ag Zn 75 25 implants fully eradicated the bacterial inoculum while the specimens from the

PT–Ag 50 group reduced the bacterial growth by 2-log ($p < 0.001$) as compared to the NT and PT implants (Fig. 6B).

3.5. Cytocompatibility of MC3T3-E1 cells on biofunctionalized implants

At day 1, the MC3T3-E1 cells cultured on all implants demonstrated similar metabolic activities while after day 3 the metabolic
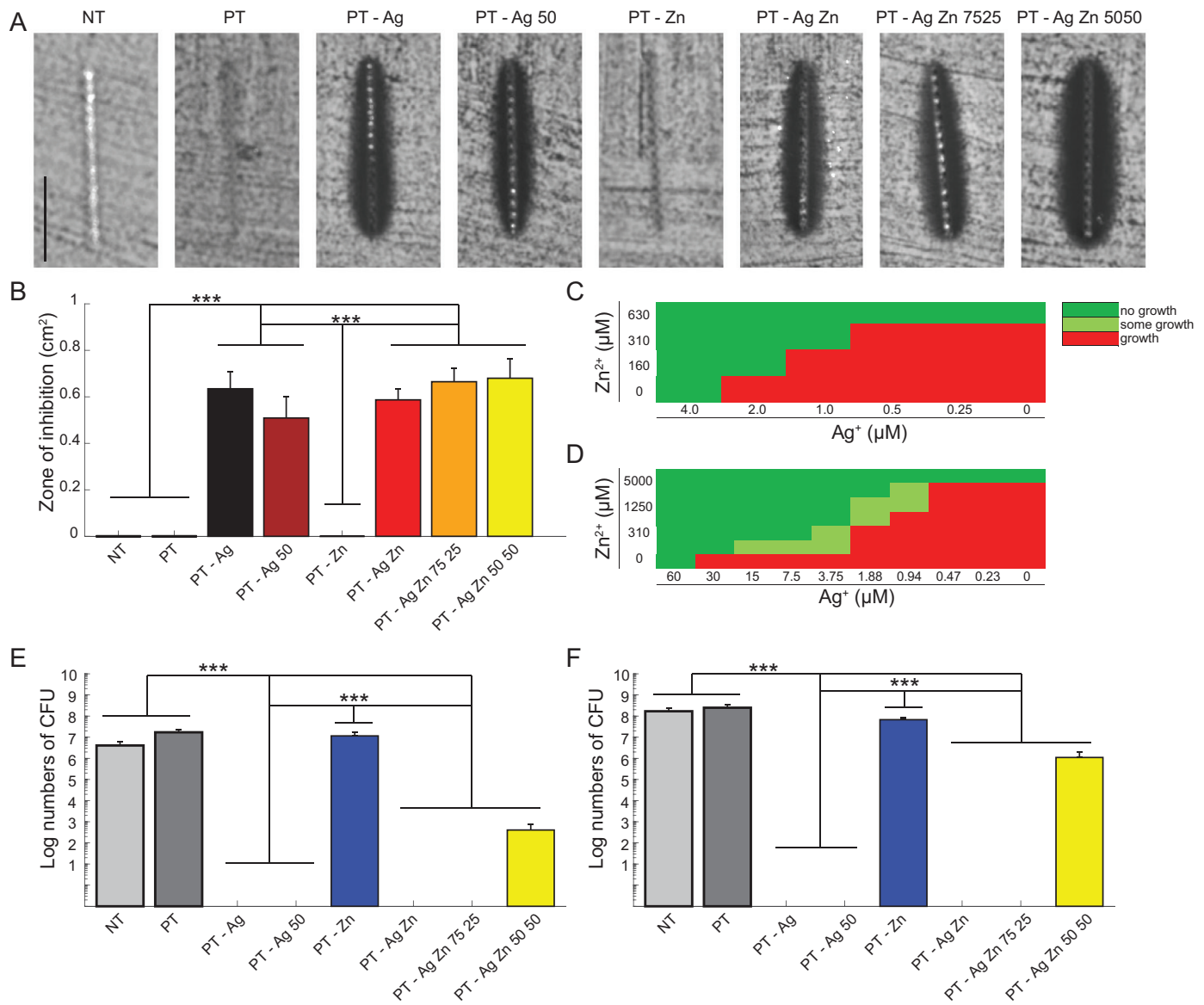
Fig. 4. The antibacterial leaching activity and quantification of bactericidal activity *in vitro* against MRSA USA300. (A) The images of the antibacterial inhibition zones around the specimens after 24 h on agar with an inoculum of 10^7 CFU/mL. (B) The quantification of the area of the inhibition zones. (C) The minimum inhibitory and (D) bactericidal concentration for the different concentrations of Ag^+ and/or Zn^{2+} ions. (E) The adherent and (F) planktonic bactericidal activity against an inoculum of 2×10^3 CFU/mL after 24 h. *, $p < 0.05$, **, $p < 0.01$, ***, $p < 0.001$. All experiments were performed in triplicates. Scale bar = 1 cm.

activity was enhanced for cells on the PT–Zn implants as compared to the PT–Ag, PT–Ag 50, and PT Ag Zn 75 25 implants ($p < 0.05$, $p < 0.05$ and $p < 0.01$, respectively; Fig. 7A). After 7 days, the metabolic activities of the cells present on the PT and PT–Zn implants were significantly higher than those of the NT implants ($p < 0.001$). Similarly, the metabolic activity of cells on the PT group was significantly higher than that of the PT–Ag, PT–Ag 50, and PT–Ag Zn 75 25 groups ($p < 0.001$, $p < 0.01$ and $p < 0.01$, respectively). The same held for the PT–Zn implants as compared to the PT–Ag, PT–Ag 50, and PT–Ag Zn 75 25 implants ($p < 0.001$). After 11 days, cells on the PT and PT–Zn groups displayed enhanced metabolic activity as compared to the NT group ($p < 0.001$). The same was observed for PT as compared to PT–Ag, PT–Ag 50, and PT–Ag Zn 75 25 ($p < 0.05$) and PT–Zn as compared to PT–Ag, PT–Ag 50, and PT–Ag Zn 75 25 ($p < 0.001$). The ALP activity did not differ significantly between the different groups after 11 days (Fig. 7B). The cell morphology after 11 days demonstrated that all

surfaces had cell attachment on significant parts of their surface (Fig. 7C). The cells showed elongated morphologies and were found to span large areas.

4. Discussion

To improve implant longevity, the prevention of IAIs induced by antibiotic-resistant bacteria is essential. Multifunctional implant surfaces that possess antibacterial activity and stimulate bony ingrowth are important tools in our quest to achieve that goal. AM enables the fabrication of highly porous implants that could benefit the most from these multifunctional surfaces, as bacteria could adhere to the internal surfaces of such porous structures and more easily survive the sterilization process. On the other hand, however, the much larger internal surface area of AM porous biomaterials amplifies the effects of the applied surface biofunctionalization. In this study, PEO biofunctionalized SLM porous titanium
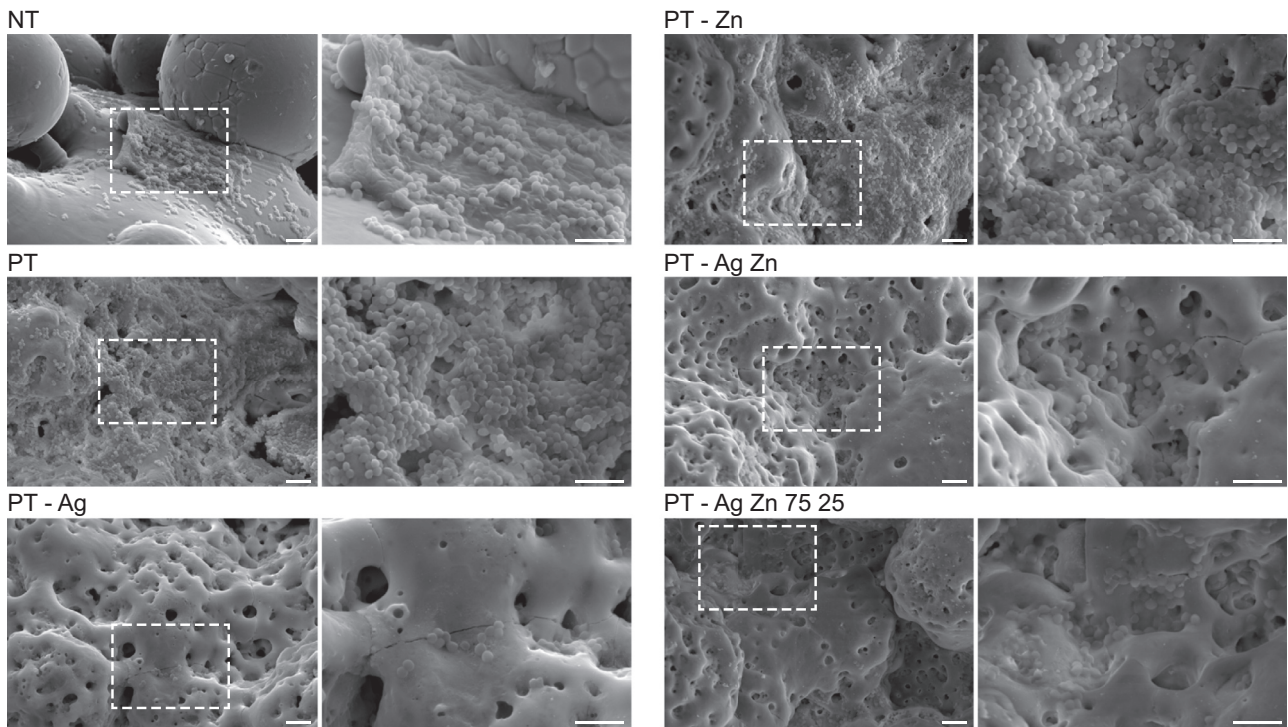
Fig. 5. Biofilm formation on the implants ($n = 2$) following 48 h incubation in TSB 1% glucose as visualized using low (2000x) and high (8000x) magnification SEM images. Scale bar = 5 μm.
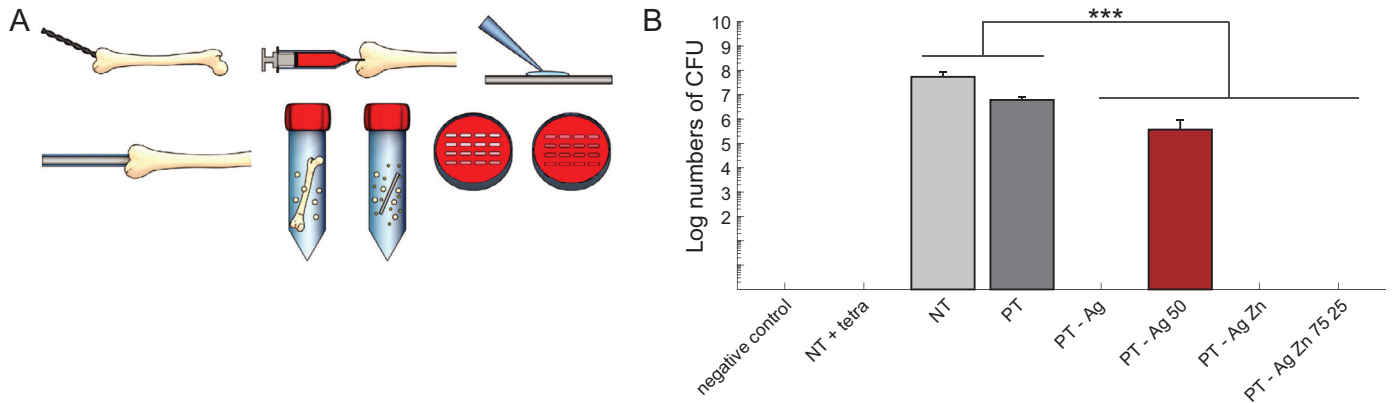
**Fig. 6.** The bactericidal activity of the implants against MRSA USA300 in an *ex vivo* femoral mouse model. (A) A 0.5 mm hole was created into the intramedullary canal of mouse femurs by drilling through the epicondyle. Thereafter, the bone marrow was removed and 2 μl PBS was injected. The mouse femurs were inoculated with 2×10^2 CFU and were implanted intramedullary. After 24 h of incubation, the femurs were homogenized and 10-fold serial dilutions of the homogenate were plated on blood agar plates. (B) The quantification of the number of CFU following 24 h incubation *ex vivo*. To confirm proper sterilization, one femur without implant and bacterial inoculum was processed and analyzed (negative control). For validation of the model, 2 μl of tetracycline was injected intramedullary prior to implantation with an inoculated implant (NT + tetra). $n = 3$, ***, $p < 0.001$.

implants bearing Ag and Zn NPs demonstrated multifunctional behavior including the prevention of colonization by MRSA both *in vitro* as well as *ex vivo* without inducing cytotoxicity, while PT–Zn implants further enhanced the metabolic activity of pre-osteoblast cells.

Currently, IAIs account for 20% of orthopedic implant failures [29]. Most strains involved in IAI displayed resistance to at least one antibiotic [30] reducing treatment rates to 48% [31] and enhancing patient morbidities [32]. With the number of patients anticipated to increase up to 600% by 2030 [33] due to an aging and increasingly obese population, these complications will continue to increase the burden for patients and society [34]. Although the need for multifunctional implant surfaces has been recognized for some time, the synthesis of surfaces that possess antibacterial ef-

ficacy and osteogenic behavior has proven to be challenging. Both properties go hand in hand, as proper bone ingrowth limits the space for bacteria to cause infection while adherent bacteria on the implant surfaces impair the proper adherence and differentiation of osteogenic cells [35]. Therefore, multifunctional surfaces should contain multiple elements to induce both antibacterial and osteogenic properties [36]. Ideally, a multifunctional surface would promote rapid osseointegration and provide both immediate and long-term protection against bacteria adhering to the implant surface as well as those present in the tissue surrounding the implant. The development of such types of surfaces in a time- and cost-efficient manner requires a single-step process that provides strong adhesion between the surface and implant substrate and is applicable to complex geometries without altering the mechanical
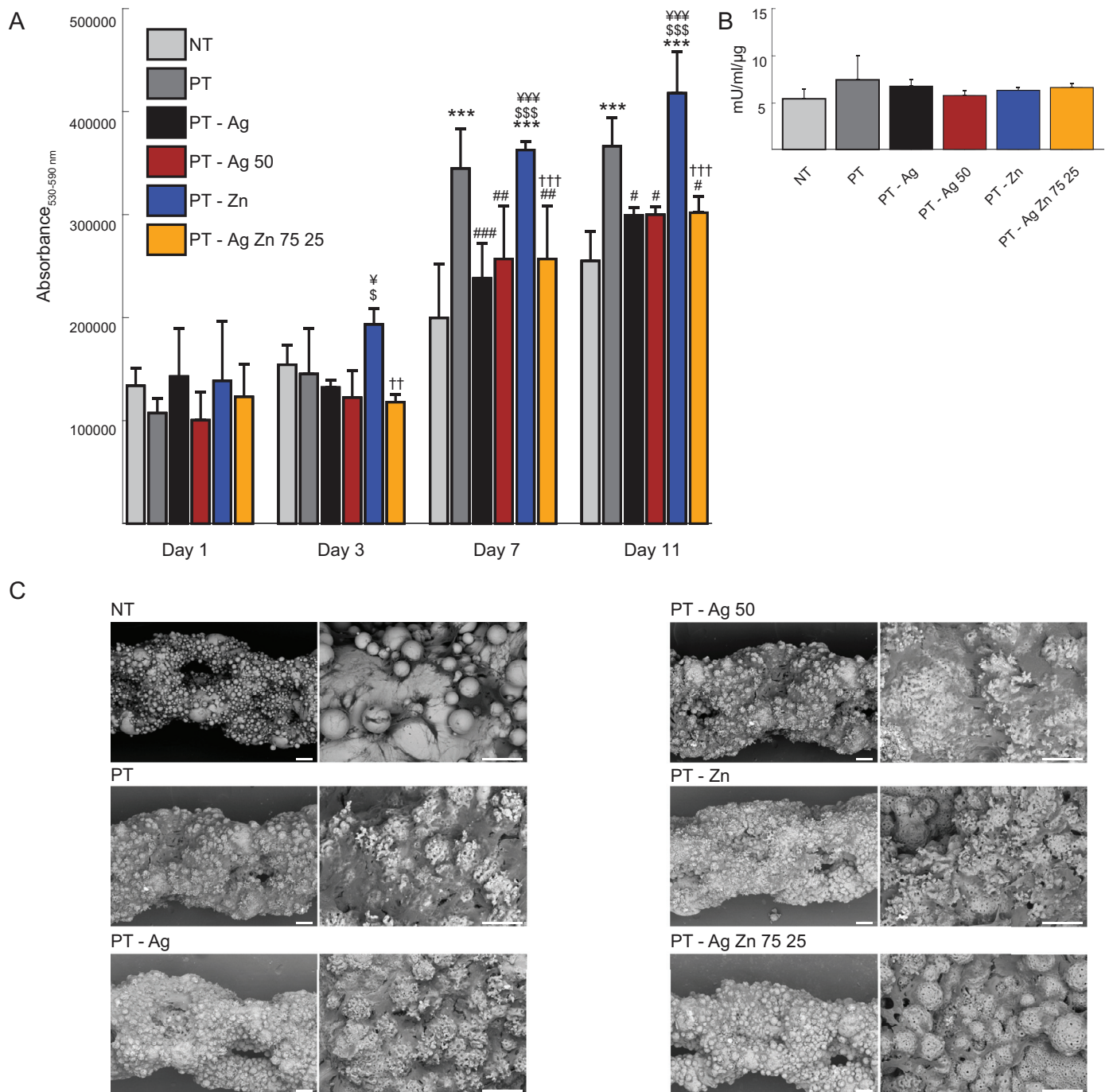
Fig. 7. Cytocompatibility assessment using MC3T3-E1 pre-osteoblasts cultured on the implants ($n = 4$). (A) The metabolic activity of the MC3T3-E1 cells indicated as the optical density ($OD_{530-590}$ nm) determined by the Presto blue assay after 1, 3, and 7 days of culture. (B) The ALP activity and (C) SEM images demonstrating the cell morphology and the spread of the MC3T3-E1 cells on the implants after 11 days of culture. *, $p < 0.05$, **, $p < 0.01$ ***, $p < 0.001$. *vs NT, # vs PT, ¥ vs PT–Ag, $ vs PT–Ag 50, † vs PT–Zn. Scale bar = 50 μm.

properties of the implant. The use of PEO with Ca/P-based electrolytes containing Ag and Zn NPs does comply with all of the abovementioned criteria [14,37,38].

While the antibacterial properties of Ag have been known for some time, there are some concerns regarding the cytotoxicity of silver-based agents [39]. Meanwhile, Zn has been applied in various forms on biofunctionalized biomaterials [40,41] and has demonstrated bactericidal activity against a wide spectrum of Gram-positive and Gram-negative bacteria [22,42-44] as well as osteogenic properties including the stimulation of the adhesion,

proliferation, and osteogenic differentiation of mesenchymal stem cells (MSCs) [45-47]. Furthermore, Zn is five times less toxic for human MSCs as compared to Ag [48,49]. However, Ag and Zn NPs have, thus far, not been incorporated collectively onto the surface of porous AM titanium implants with vast surface areas to fully exploit the aforementioned properties of Ag and Zn NPs.

The biofunctionalized implants in this study released Zn^{2+} and Ag^+ ions for up to 28 days. The addition of Zn NPs to the PEO electrolyte resulted in a reduced rate of Ag^+ released from the PT–Ag Zn implants as compared to the PT–Ag group. This observation

may originate from a reduced incorporation of Ag NP onto the implant surface or a reduced rate of Ag^+ oxidation and subsequent release due to galvanic coupling [46,50]. Since Zn has a lower standard electrode potential as compared to both Ag and the TiO_2 surface layer [51], the Zn NPs will function as local anodes, Ag NP as local cathodes, and the TiO_2 surface layer as the electron pathway, ultimately resulting in the oxidation of the Zn NP and subsequent Zn^{2+} release. The oxidation of Ag NP and, thus, the release of Ag^+ is, however, inhibited. Simultaneously, H^+ will be consumed from the surrounding environment during the micro-galvanic coupling process, which disturbs the ATP synthesis and ion transportation inside bacteria, thereby contributing to the creation of an antibacterial zone in the proximity of the implant surface [51].

The ion release from the implant surface results in an antibacterial leaching behavior, which in this study is reflected by the zone of inhibition. We observed that the PT–Ag and PT–Ag Zn implants exhibited a significant zone of inhibition, whereas the PT–Zn implants did not, which concurs with the fact that the MIC of Zn^{2+} is 100 to 150 times higher than that of Ag^+ [52]. We also observed that combining Zn^{2+} and Ag^+ allowed to reduce the Ag^+ concentration by up to 120 folds while keeping similar MIC and MBC values, respectively.

Zn is less toxic for bacteria than Ag. That is because Zn is crucial in various bacterial metabolic processes, such as ATP synthesis, and has been shown to play a role in inter-bacterial communication between *Staphylococci* resulting in enhanced bacterial adhesion and biofilm formation [53, 54]. In contrast, Ag is not vital for bacterial cells and irreversibly targets cytoplasmic proteins, enzymatic functioning, and the DNA replication machinery resulting in cell death [55–57]. The exact mechanism underlying the synergistic antibacterial behavior between Zn and Ag is not fully understood. However, ROS may play a role in the observed synergistic antibacterial behavior between Zn^{2+} and Ag^+ [58, 59].

Due to their short-life time, however, ROS do not enhance the leaching activity of the implants. Instead, they ward off bacteria that attach to the surface. All PEO biofunctionalized implants in this study generated hydroxyl radicals whereas NT implants did not. This suggests that the formation of rutile and anatase TiO_2 phases during the PEO process contributes to ROS generation [14], which has been shown to prevent bacterial adhesion [60]. The PT–Zn implants generated the highest levels of hydroxyl and methyl radical generation, followed by the PT–Ag implants whereas the combinations of Ag and Zn ratios reduced the amount of the hydroxyl radical formed and annihilated the formation of methyl radicals. Ag doping of Zn photocatalytic microspheres has demonstrated to enhance the formation of hydroxyl radicals [61,62]. However, the exact mechanisms through which the biofunctionalization of SLM titanium implants with both Ag and Zn NPs affects the formation of ROS as compared to either nanoparticles species alone are not clear and need to be elucidated.

Infection with MRSA worsens the patient's prognosis compared to methicillin-susceptible *Staphylococcus aureus* strains [63]. It is, therefore, relevant to test biofunctionalized implants in an adequate model against MRSA. Therefore, we investigated the antibacterial activity in a murine *ex vivo* model to simulate *in vivo* conditions. Although *ex vivo* models lack an active immune system and the ability of bony ingrowth, the bone extracellular matrix has shown to greatly support the adhesion of *Staphylococcus aureus* and, thus, affect the infection process [64]. In this model, the PT–Ag, PT–Ag Zn, and PT–Ag Zn 75 25 implants fully eradicated a bacterial inoculum within 24 h, whereas the PT–Ag 50 implants induced a two-log reduction in the number of CFU as compared to the PT and PT–Zn groups.

In addition to improving the antibacterial properties of the implants, the addition of Zn to Ag-bearing surfaces is important to reduce the cytotoxicity caused by Ag. In our study, the PT–Zn implants enhanced the metabolic activity of the MC3T3-E1 cells after 3, 7, and 11 days as compared to NT and Ag-biofunctionalized implants, while no difference in the ALP expression was detected after 11 days. Our results are partially in line with previous studies that have demonstrated the effects of such ions on both cell adhesion and osteogenic differentiation *in vitro* [65,66] and have been shown to correlate with enhanced bone ingrowth *in vivo* [24]. Taken together, the results of the current study suggest that the dose of Zn^{2+} on our implants might have been too low to initiate a clear effect on the ALP activity or that these effects may be present at other time points. Meanwhile, the cytotoxicity of Ag has shown to differ between *in vitro* and *in vivo* experiments and can affect the proper functioning of neutrophils [20,67]. Combining Ag and Zn in a plasma sprayed hydroxyapatite coating has resulted in enhanced bone regeneration in orthopedic and dental *in vivo* models [68]. Titanium biomaterials biofunctionalized by PEO through the addition of Ag NPs have thus far not been investigated *in vivo* while PEO-biofunctionalized biomaterials with Ca/P electrolyte [15,69] as well as with Zn [70,71] have both shown to stimulate osseointegration. Further *in vivo* studies are, therefore, required to take the next steps in translating the results of the current study to clinical settings.

Altogether, the number of AM porous implants is anticipated to increase substantially. The prevention of infection associated with such types of implants is, therefore, crucial. Given that over 60% of IAIs are induced by *Staphylococci* [6], and *S. aureus* and *S. epidermidis* strains exhibit ever increasing levels of antibiotic-resistance [72-74], the current prophylaxis regimes are becoming less effective [7], thereby putting patients at risk and warranting the development of novel strategies to prevent IAIs by resistant bacteria. One of the most important strategies in this regard is the surface biofunctionalization of AM implants with Ag and Zn NPs. Combining Ag and Zn results in synergistic antibacterial behavior [50,75,76], which allows for reducing the required concentration of Ag ions by two orders of magnitude and is likely caused by a combination of ion release and ROS formation on the implant surface. This will make the development of bacterial resistance unlikely, which is crucial to prevent future infections on AM porous implants.

5. Conclusions

To improve the longevity of orthopedic implants, multifunctional implant surfaces that both prevent bacterial infection and strengthen the fixation of the implant inside the host bony tissue are being developed. Here, we designed and synthesized highly porous SLM titanium bone implants that were biofunctionalized using PEO with Ag and Zn NPs in ratios from 0 to 100%. The biofunctionalized implants with ratios of up to 75% Ag and 25% Zn fully eradicated bacterial inocula within 24 h in both *in vitro* and *ex vivo* experiments. Combining Ag and Zn NPs on the implant surface resulted in reduced rates of Ag ion release and ROS formation. Furthermore, the Zn-biofunctionalized implants enhanced the metabolic activity of pre-osteoblast cells as compared to the NT and Ag-biofunctionalized implants. Therefore, the implants biofunctionalized with Ag and Zn NPs hold great promise as candidates for further development towards multifunctional bone implants.

Declaration of Competing Interest

The authors declare that they have no known competing financial interests or personal relationships that could have appeared to influence the work reported in this paper.

Acknowledgements

The research for this paper was financially supported by the Prosperos project, funded by the Interreg VA Flanders – The Netherlands program, CCI grant no. 2014TC16RFCB046.

References

[1] M. Khan, K. Osman, G. Green, F.S. Haddad, The epidemiology of failure in total knee arthroplasty, Bone Joint J. 98–B (2016) 105–112.

[2] E. Lenguerrand, M.R. Whitehouse, A.D. Beswick, S.A. Jones, M.L. Porter, A.W. Blom, Revision for prosthetic joint infection following hip arthroplasty, Bone Joint Res. 6 (2017) 391–398.

[3] B.H. Kapadia, R.A. Berg, J.A. Daley, J. Fritz, A. Bhave, M.A. Mont, Periprosthetic joint infection, The Lancet 387 (2016) 386–394.

[4] C.R. Arciola, D. Campoccia, G.D. Ehrlich, L. Montanaro, Biofilm-based implant infections in orthopaedics, Adv. Exp. Med. Biol. 1 (2015) 29–46.

[5] L. Hall-Stoodley, J.W. Costerton, P. Stoodley, Bacterial biofilms: from the natural environment to infectious diseases, Nat. Rev. Microbiol. 2 (2004) 95–108.

[6] D. Campoccia, L. Montanaro, C.R. Arciola, The significance of infection related to orthopedic devices and issues of antibiotic resistance, Biomaterials 27 (2006) 2331–2339.

[7] B. Li, T.J. Webster, Bacteria antibiotic resistance: new challenges and opportunities for implant-associated orthopedic infections, J. Orthop. Res. 36 (2017) 22–32.

[8] K.L. Garvin, S.H. Hinrichs, U. J.A., Emerging antibiotic-resistant bacteria. Their treatment in total joint arthroplasty, Clin. Orthop. Relat. Res. 369 (1999) 110–123.

[9] J. Parvizi, I.M. Pawasarat, K.A. Azzam, A. Joshi, E.N. Hansen, K.J. Bozic, Periprosthetic joint infection, J Arthroplasty 25 (2010) 103–107.

[10] K.R. Berend, A.V. Lombardi, M.J. Morris, A.G. Bergeson, J.B. Adams, M.A. Sneller, Two-stage treatment of hip periprosthetic joint infection is associated with a high rate of infection control but high mortality, Clin. Orthop. Relat. Res. 471 (2012) 510–518.

[11] A. Zadpoor, Design for additive bio-manufacturing: from patient-specific medical devices to rationally designed meta-biomaterials, Int J Mol Sci 18 (2017).

[12] S. Ahmadi, S. Yavari, R. Wauthle, B. Pouran, J. Schrooten, H. Weinans, A. Zadpoor, Additively manufactured open-cell porous biomaterials made from six different space-filling unit cells: the mechanical and morphological properties, Materials (Basel) 8 (2015) 1871–1896.

[13] F.S.L. Bobbert, K. Lietaert, A.A. Eftekhari, B. Pouran, S.M. Ahmadi, H. Weinans, A.A. Zadpoor, Additively manufactured metallic porous biomaterials based on minimal surfaces: a unique combination of topological, mechanical, and mass transport properties, Acta Biomater 53 (2017) 572–584.

[14] I.A.J. van Hengel, M. Riool, L.E. Fratila-Apachitei, J. Witte-Bouma, E. Farrell, A.A. Zadpoor, S.A.J. Zaat, I. Apachitei, Selective laser melting porous metallic implants with immobilized silver nanoparticles kill and prevent biofilm formation by methicillin-resistant Staphylococcus aureus, Biomaterials 140 (2017) 1–15.

[15] C.-J. Chung, R.-.T. Su, H.-.J. Chu, H.-.T. Chen, H.-.K. Tsou, J.-.L. He, Plasma electrolytic oxidation of titanium and improvement in osseointegration, J. Biomed. Mater. Res. Part B: Appl. Biomater. 101B (2013) 1023–1030.

[16] J.S. Kim, E. Kuk, K.N. Yu, J.-.H. Kim, S.J. Park, H.J. Lee, S.H. Kim, Y.K. Park, Y.H. Park, C.-.Y. Hwang, Y.-.K. Kim, Y.-.S. Lee, D.H. Jeong, M.-.H. Cho, Antimicrobial effects of silver nanoparticles, nanomedicine: nanotechnology, Bio. Med. 3 (2007) 95–101.

[17] A. Nanda, M. Saravanan, Biosynthesis of silver nanoparticles from staphylococcus aureus and its antimicrobial activity against MRSA and MRSE, nanomedicine: nanotechnology, Bio. Med. 5 (2009) 452–456.

[18] G. Franci, A. Falanga, S. Galdiero, L. Palomba, M. Rai, G. Morelli, M. Galdiero, Silver nanoparticles as potential antibacterial agents, Molecules 20 (2015) 8856–8874.

[19] A. Panacek, L. Kvitek, M. Smekalova, R. Vecerova, M. Kolar, M. Roderova, F. Dycka, M. Sebela, R. Prucek, O. Tomanec, R. Zboril, Bacterial resistance to silver nanoparticles and how to overcome it, Nat. Nanotechnol. 13 (2018) 65–71.

[20] M. Croes, S. Bakhshandeh, I.A.J. van Hengel, K. Lietaert, K.P.M. van Kessel, B. Pouran, B.C.H. van der Wal, H.C. Vogely, W. Van Hecke, A.C. Fluit, C.H.E. Boel, J. Alblas, A.A. Zadpoor, H. Weinans, S. Amin Yavari, Antibacterial and immunogenic behavior of silver coatings on additively manufactured porous titanium, Acta Biomater. 81 (2018) 315–327.

[21] N. Duran, M. Duran, M.B. de Jesus, A.B. Seabra, W.J. Favaro, G. Nakazato, Silver nanoparticles: a new view on mechanistic aspects on antimicrobial activity, Nanomedicine 12 (2016) 789–799.

[22] A. Sirelkhatim, S. Mahmud, A. Seeni, N.H.M. Kaus, L.C. Ann, S.K.M. Bakhori, H. Hasan, D. Mohamad, Review on zinc oxide nanoparticles: antibacterial activity and toxicity mechanism, Nanomicro. Lett. 7 (2015) 219–242.

[23] X. Shen, Y. Hu, G. Xu, W. Chen, K. Xu, Q. Ran, P. Ma, Y. Zhang, J. Li, K. Cai, Regulation of the biological functions of osteoblasts and bone formation by Zn-incorporated coating on microrough titanium, ACS Appl. Mater. Interfaces 6 (2014) 16426–16440.

[24] Y. Qiao, W. Zhang, P. Tian, F. Meng, H. Zhu, X. Jiang, X. Liu, P.K. Chu, Stimulation of bone growth following zinc incorporation into biomaterials, Biomaterials 35 (2014) 6882–6897.

[25] B.S. Necula, J.P.T.M. van Leeuwen, L.E. Fratila-Apachitei, S.A.J. Zaat, I. Apachitei, J. Duszczyk, In vitro cytotoxicity evaluation of porous TiO$_2$–Ag antibacterial coatings for human fetal osteoblasts, Acta Biomater. 8 (2012) 4191–4197.

[26] L. Lara Rodriguez, P.A. Sundaram, E. Rosim-Fachini, A.M. Padovani, N. Diffoot-Carlo, Plasma electrolytic oxidation coatings on γTiAl alloy for potential biomedical applications, J. Biomed. Mater. Res. Part B: Appl. Biomater. 102 (2014) 988–1001.

[27] B.S. Necula, L.E. Fratila-Apachitei, S.A.J. Zaat, I. Apachitei, J. Duszczyk, In vitro antibacterial activity of porous TiO$_2$–Ag composite layers against methicillin-resistant staphylococcus aureus, Acta Biomater. 5 (2009) 3573–3580.

[28] F.C. Tenover, R.V. Goering, Methicillin-resistant staphylococcus aureus strain USA300: origin and epidemiology, J Antimicrob Chemother 64 (2009) 441–446.

[29] K.J. Bozic, S.M. Kurtz, E. Lau, K. Ong, T.P. Vail, D.J. Berry, The epidemiology of revision total hip arthroplasty in the United States, J. Bone Joint. Surg. Am. 91 (2009) 128–133.

[30] C.R. Arciola, D. Campoccia, Y.H. An, L. Baldassarri, V. Pirini, M.E. Donati, F. Pegreffi, L. Montanaro, Prevalence and antibiotic resistance of 15 minor staphylococcal species colonizing orthopedic implants, Int. J. Artif. Organs 29 (2006) 395–401.

[31] D.J. Kilgus, D.J. Howe, A. Strang, Results of periprosthetic hip and knee infections caused by resistant bacteria, Clin. Orthop. Relat. Res. 404 (2002) 116–124.

[32] S. Inoue, T. Moriyama, Y. Horinouchi, T. Tachibana, F. Okada, K. Maruo, S. Yoshiya, Comparison of clinical features and outcomes of staphylococcus aureus vertebral osteomyelitis caused by methicillin-resistant and methicillin-sensitive strains, Springerplus 2 (2013) 1–7.

[33] S. Kurtz, K. Ong, E. Lau, F. Mowat, M. Halpern, Projections of primary and revision hip and knee arthroplasty in the United States from 2005 to 2030, J. Bone Joint. Surg. Am. 89 (2007) 780–785.

[34] S.M. Kurtz, E. Lau, H. Watson, J.K. Schmier, J. Parvizi, Economic burden of periprosthetic joint infection in the United States, J Arthroplasty 27 (2012) 61–65.

[35] A.G. Gristina, P. Naylor, Q. Myrvik, Infections from biomaterials and implants: a race for the surface, Med. Prog. Technol. 14 (1989) 205–224.

[36] J. Raphel, M. Holodniy, S.B. Goodman, S.C. Heilshorn, Multifunctional coatings to simultaneously promote osseointegration and prevent infection of orthopaedic implants, Biomaterials 84 (2016) 301–314.

[37] B.S. Necula, I. Apachitei, F.D. Tichelaar, L.E. Fratila-Apachitei, J. Duszczyk, An electron microscopical study on the growth of TiO$_2$–Ag antibacterial coatings on Ti6Al7Nb biomedical alloy, Acta Biomater. 7 (2011) 2751–2757.

[38] Z. Gorgin Karaji, R. Hedayati, B. Pouran, I. Apachitei, A.A. Zadpoor, Effects of plasma electrolytic oxidation process on the mechanical properties of additively manufactured porous biomaterials, Mater. Sci. Eng. C Mater. Biol. Appl. 76 (2017) 406–416.

[39] C.E. Albers, W. Hofstetter, K.A. Siebenrock, R. Landmann, F.M. Klenke, In vitro cytotoxicity of silver nanoparticles on osteoblasts and osteoclasts at antibacterial concentrations, Nanotoxicology 7 (2013) 30–36.

[40] Y. Su, K. Wang, J. Gao, Y. Yang, Y.X. Qin, Y. Zheng, D. Zhu, Enhanced cytocompatibility and antibacterial property of zinc phosphate coating on biodegradable zinc materials, Acta Biomater. (2019) 174–185.

[41] R. Zhang, X. Liu, Z. Xiong, Q. Huang, X. Yang, H. Yan, J. Ma, Q. Feng, Z. Shen, Novel micro/nanostructured TiO$_2$/ZnO coating with antibacterial capacity and cytocompatibility, Ceram Int 44 (2018) 9711–9719.

[42] N. Jones, B. Ray, K.T. Ranjit, A.C. Manna, Antibacterial activity of ZnO nanoparticle suspensions on a broad spectrum of microorganisms, FEMS Microbiol Lett 279 (2008) 71–76.

[43] A. Jesline, N.P. John, P.M. Narayanan, C. Vani, S. Murugan, Antimicrobial activity of zinc and titanium dioxide nanoparticles against biofilm-producing methicillin-resistant staphylococcus aureus, Appl. Nanosci. 5 (2014) 157–162.

[44] U. Kadiyala, E.S. Turali-Emre, J.H. Bahng, N.A. Kotov, J.S. VanEpps, Unexpected insights into antibacterial activity of zinc oxide nanoparticles against methicillin resistant staphylococcus aureus (MRSA), Nanoscale 10 (2018) 4927–4939.

[45] H. Hu, W. Zhang, Y. Qiao, X. Jiang, X. Liu, C. Ding, Antibacterial activity and increased bone marrow stem cell functions of Zn-incorporated TiO$_2$ coatings on titanium, Acta Biomater 8 (2012) 904–915.

[46] G. Jin, H. Cao, Y. Qiao, F. Meng, H. Zhu, X. Liu, Osteogenic activity and antibacterial effect of zinc ion implanted titanium, Colloids Surf. B Biointerfaces 117 (2014) 158–165.

[47] Y. Yu, G. Jin, Y. Xue, D. Wang, X. Liu, J. Sun, Multifunctions of dual Zn/Mg ion co-implanted titanium on osteogenesis, angiogenesis and bacteria inhibition for dental implants, Acta Biomater 49 (2017) 590–603.

[48] S. Hackenberg, A. Scherzed, M. Kessler, S. Hummel, A. Technau, K. Froelich, C. Ginzkey, C. Koehler, R. Hagen, N. Kleinsasser, Silver nanoparticles: evaluation of DNA damage, toxicity and functional impairment in human mesenchymal stem cells, Toxicol. Lett. 201 (2011) 27–33.

[49] P. Ickrath, M. Wagner, A. Scherzad, T. Gehrke, M. Burghartz, R. Hagen, K. Radeloff, N. Kleinsasser, S. Hackenberg, Time-dependent toxic and genotoxic effects of zinc oxide nanoparticles after long-term and repetitive exposure to human mesenchymal stem cells, Int. J. Environ. Res. Public Health 14 (2017).

[50] G. Jin, H. Qin, H. Cao, S. Qian, Y. Zhao, X. Peng, X. Zhang, X. Liu, P.K. Chu, Synergistic effects of dual Zn/Ag ion implantation in osteogenic activity and antibacterial ability of titanium, Biomaterials 35 (2014) 7699–7713.

[51] H. Cao, X. Liu, F. Meng, P.K. Chu, Biological actions of silver nanoparticles embedded in titanium controlled by micro-galvanic effects, Biomaterials 32 (2011) 693–705.

[52] S. Ferraris, S. Spriano, Antibacterial titanium surfaces for medical implants, Mater. Sci. Eng. C Mater. Biol. Appl. 61 (2016) 965–978.

[53] D. He, C.J. Miller, T.D. Waite, Fenton-like zero-valent silver nanoparticle-mediated hydroxyl radical production, J. Catal. 317 (2014) 198–205.

[54] D.G. Conrady, C.C. Brescia, K. Horii, A.A. Weiss, D.J. Hassett, A.B. Herr, A zinc-dependent adhesion module is responsible for intercellular adhesion in staphylococcal biofilms, Proc. Natl. Acad. Sci. U.S.A. 105 (2008) 19456–19461.

[55] T.C. Dakal, A. Kumar, R.S. Majumdar, V. Yadav, Mechanistic basis of antimicrobial actions of silver nanoparticles, Front Microbiol. 7 (2016) 1831.

[56] L. Wang, C. Hu, L. Shao, The antimicrobial activity of nanoparticles: present situation and prospects for the future, Int. J. Nanomed. 12 (2017) 1227–1249.

[57] M. Rai, A.P. Ingle, R. Pandit, P. Paralikar, I. Gupta, M.V. Chaud, C.A. Dos Santos, Broadening the spectrum of small-molecule antibacterials by metallic nanoparticles to overcome microbial resistance, Int. J. Pharm. 532 (2017) 139–148.

[58] T. Wei, Q. Yu, H. Chen, Responsive and synergistic antibacterial coatings: fighting against bacteria in a smart and effective way, Adv. Healthc. Mater. 8 (2019).

[59] X. Wang, S. Liu, M. Li, P. Yu, X. Chu, L. Li, G. Tan, Y. Wang, X. Chen, Y. Zhang, C. Ning, The synergistic antibacterial activity and mechanism of multicomponent metal ions-containing aqueous solutions against Staphylococcus aureus, J Inorg Biochem 163 (2016) 214–220.

[60] B. Del Curto, M.F. Brunella, C. Giordano, M.P. Pedeferri, V. Valtulina, L. Visai, A. Cigada, Decreased bacterial adhesion to surface-treated titanium, Int J Artif Organs 28 (2005) 718–730.

[61] W. Lu, S. Gao, J. Wang, One-pot synthesis of Ag/ZnO self-assembled 3D hollow microspheres with enhanced photocatalytic performance, J. Phys. Chem. C 112 (2008) 16792–16800.

[62] O. Bechambi, M. Chalbi, W. Najjar, S. Sayadi, Photocatalytic activity of ZnO doped with Ag on the degradation of endocrine disrupting under UV irradiation and the investigation of its antibacterial activity, Appl Surf Sci 347 (2015) 414–420.

[63] D. Teterycz, T. Ferry, D. Lew, R. Stern, M. Assal, P. Hoffmeyer, L. Bernard, I. Uckay, Outcome of orthopedic implant infections due to different staphylococci, Int. J. Infect. Dis. 14 (2010) 913–918.

[64] M.C. Hudson, W.K. Ramp, K.P. Frankenburg, Staphylococcus aureus adhesion to bone matrix, FEMS Microbiol. Lett. 173 (1999) 279–284.

[65] K. Yusa, O. Yamamoto, M. Fukuda, S. Koyota, Y. Koizumi, T. Sugiyama, In vitro prominent bone regeneration by release zinc ion from Zn-modified implant, Biochem. Biophys. Res. Commun. 412 (2011) 273–278.

[66] Z. Zhang, B. Gu, W. Zhang, G. Kan, J. Sun, The enhanced characteristics of osteoblast adhesion to porous Zinc–TiO$_2$ coating prepared by plasma electrolytic oxidation, Appl. Surf. Sci. 258 (2012) 6504–6511.

[67] S. Bakhshandeh, Z. Gorgin Karaji, K. Lietaert, A.C. Fluit, C.H.E. Boel, H.C. Vogely, T. Vermonden, W.E. Hennink, H. Weinans, A.A. Zadpoor, S. Amin Yavari, Simultaneous delivery of multiple antibacterial agents from additively manufactured porous biomaterials to fully eradicate planktonic and adherent Staphylococcus aureus, ACS Appl. Mater. Interfaces 9 (2017) 25691–25699.

[68] A.A. Vu, S.F. Robertson, D. Ke, A. Bandyopadhyay, S. Bose, Mechanical and biological properties of ZnO, SiO$_2$, and Ag$_2$O doped plasma sprayed hydroxyapatite coating for orthopaedic and dental applications, Acta Biomater. 92 (2019) 325–335.

[69] A. Santos-Coquillat, E. Martínez-Campos, M. Mohedano, R. Martínez-Corriá, V. Ramos, R. Arrabal, E. Matykina, In vitro and in vivo evaluation of PEO-modified titanium for bone implant applications, Surface Coat. Technol. 347 (2018) 358–368.

[70] J. He, W. Feng, B.H. Zhao, W. Zhang, Z. Lin, In vivo effect of titanium implants with porous zinc-containing coatings prepared by plasma electrolytic oxidation method on osseointegration in rabbits, Int. J. Oral. Maxillofac. Implants 33 (2018) 298–310.

[71] Q. Zhao, L. Yi, L. Jiang, Y. Ma, H. Lin, J. Dong, Surface functionalization of titanium with zinc/strontium-doped titanium dioxide microporous coating via microarc oxidation, Nanomedicine 16 (2019) 149–161.

[72] S. Ravi, M. Zhu, C. Luey, S.W. Young, Antibiotic resistance in early periprosthetic joint infection, ANZ J. Surg. 86 (2016) 1014–1018.

[73] A.M. Malhas, R. Lawton, M. Reidy, D. Nathwani, B.A. Clift, Causative organisms in revision total hip & knee arthroplasty for infection: increasing multi-antibiotic resistance in coagulase-negative Staphylococcus and the implications for antibiotic prophylaxis, Surgeon 13 (2015) 250–255.

[74] A. Bogut, J. Niedzwiadek, D. Strzelec-Nowak, J. Blacha, T. Mazurkiewicz, W. Marczynski, M. Koziol-Montewka, Infectious prosthetic hip joint loosening: bacterial species involved in its aetiology and their antibiotic resistance profiles against antibiotics recommended for the therapy of implant-associated infections, New Microbiol. 37 (2014) 209–218.

[75] G. Jin, H. Qin, H. Cao, Y. Qiao, Y. Zhao, X. Peng, X. Zhang, X. Liu, P.K. Chu, Zn/Ag micro-galvanic couples formed on titanium and osseointegration effects in the presence of S. aureus, Biomaterials 65 (2015) 22–31.

[76] L. Zhang, Q. Gao, Y. Han, Zn and Ag Co-doped anti-microbial TiO$_2$ coatings on Ti by micro-arc oxidation, J. Mater. Sci. Technol. 32 (2016) 919–924.